Self-assembly of an antireflective moth-like structure using antibody-functionalized nanowires and nanopore arrays

2011 Nanotechnology 22 475601

(http://iopscience.iop.org/0957-4484/22/47/475601)

Nanotechnology **22** (2011) 475601 (10pp) doi:10.1088/0957-4484/22/47/475601

Self-assembly of an antireflective moth-like structure using antibody-functionalized nanowires and nanopore arrays

Yu-Shiun Chen[1], Ning Hung[1], Li-Jen Chou[2], Jin-Chern Chiou[3], Meng-Yen Hong[1] and G Steven Huang[1,4]

[1] Department of Materials Science and Engineering, National Chiao Tung University, 1001 University Road, Hsinchu 300, Taiwan, Republic of China
[2] Department of Material Engineering, National Tsing Hua University, 101 Section 2 Kuang Fu Road, Hsinchu 30013, Taiwan, Republic of China
[3] Institute of Electrical Control Engineering, National Chiao Tung University, 1001 University Road, EE772, Hsinchu 300, Taiwan, Republic of China

E-mail: gstevehuang@mail.nctu.edu.tw

Received 9 August 2011, in final form 10 October 2011
Published 2 November 2011
Online at stacks.iop.org/Nano/22/475601

Abstract
A novel framework to fabricate moth-like nanopillar arrays was proposed. In this scheme, nanowires were first cross-linked with anti-gold nanoparticle (GNP) antibodies and mixed with the nanopore array pre-deposited by GNP, which was then followed by centrifugation. An optimal success rate of 95% was finally obtained by choosing nanorods with an aspect ratio of 5:1 by modifying with 10 ng mL^{-1} antibodies, and by inserting them into a pore array pre-deposited with 54.4 μM GNP. The nanopillar arrays thus fabricated showed high levels of antireflective efficiency across a broad wavelength. Here we demonstrate the assembly of nanowires and nanopores into nanopillar arrays by the assistance of antibody–antigen binding. The application of bio-nano-interaction provides an economic, time-saving, and throughput approach to manipulating objects on the nanoscale.

(Some figures may appear in colour only in the online journal)

1. Introduction

Nanopillar arrays have been developed to form transition layers that act to suppress reflection in optical and opto-electronic devices, such as solar cells, displays and light sensors [1–7]. Nanopillar arrays are characterized by subwavelength structures (SWSs), referred to as moth-eye structures. Many lithographic processes, such as photolithography [8], electron-beam lithography [9], nanoimprint lithography [10] and laser interference lithography [11], may be used to fabricate antireflective SWSs. A reactive ion etching process, combined with self-assembled masks composed of colloidal nanospheres [12], anodic porous alumina membranes [13] or metal particles [14, 15], has been used to fabricate SWS surfaces using a bottom-up approach. In addition, the transfer of cracked nanowires onto a flexible adhesive substrate [16] and the embedding of CdS nanowires into polycrystalline Cd–Te thin films further facilitate the practical application of nanopillar arrays [7].

Recent advances in the hierarchical assembly of functional nanodevices from nanoclusters have pointed towards potential applications in electronics and medicine [17–21]. The assembly of one-dimensional nanostructures such as nanowires has been facilitated by physical techniques, such as polarization of nanowires in an applied alternating electric field [22, 23], alignment of nanowires by a magnetic field generated by a cylindrical coaxial magnet [24] and microfluidic flows, with the control of average separation and by combining fluidic alignment with surface-patterning techniques [25, 26]. Bio-guided fabrication techniques have been developed that incorporate the characteristic self-assembling properties of

[4] Address for correspondence: Department of Materials Science and Engineering, National Chiao Tung University, 1001 University Road, Hsinchu 300, Taiwan, Republic of China.

biomaterials [17]. However, this application is limited to self-assembly of oligonucleotides or to applications involving zero-dimensional nanomaterials. The application of specific bio-nano-interactions to manipulate heterogeneous nanomaterials of higher dimensions in multiple components has yet to be explored.

2. Materials and methods

2.1. Synthesis of gold nanoparticles and anti-GNP antibodies

GNPs with diameters between 2 and 17 nm were synthesized as previously reported [27]. The synthesis of gold nanoparticles by citrate reduction involves the use of auric acid, sodium citrate and water. The nucleation and growth of GNPs through standard citrate reduction in boiling water was induced by varying the molar ratio of sodium citrate to auric acid. First, 20 mL of 1.0 mM $HAuCl_4$ was added to a 50 mL Erlenmeyer flask with a magnetic stir bar on a stirring hot plate and the solution was brought to a boil. When the boiling point was reached, 2 mL of a 1% solution of trisodium citrate dehydrate was added and gold nanoparticles gradually began to form. The sizes of the synthesized GNPs were verified by electron microscopy and atomic force microscopy [28, 29].

Anti-GNP antibodies were produced by immunizing BALB/C mice with 5 nm GNP followed by the generation of monoclonal antibodies [30]. The binding affinity and selectivity of these antibodies were characterized by an enzyme-linked immunosorbent assay (ELISA) [31, 32]. The antibodies exhibited a binding affinity highly selective for GNPs ranging from 2 to 7 nm in size and maximally so at 5 nm [29].

2.2. Single-crystal silicon nanowires

Single-crystal silicon nanowires [33] were synthesized using high-quality single-crystal wafers via a vapor–liquid–solid growth mechanism, as previously described from single-crystal (111) Si wafers (figure 1). The cleaned wafers were transferred into a high-vacuum e-beam deposition system to deposit 2 nm Au thin films at a growth rate of 0.01 nm s^{-1}. The samples were HF-cleaned before being loading into a horizontal one-zone furnace at a pressure of 10^{-2} Torr. The samples were purged with 100 sccm of high-purity argon gas at 800 °C. The argon gas was then replaced as the carrier gas by pure hydrogen gas previously saturated with liquid $SiCl_4$ at room temperature and reacted at a flow rate of 100 sccm for 30 min.

2.3. Nanopore array

Electrochemical anodization was carried out at a constant voltage of 10 V in a solution of H_3PO_4–HNO_3–H_2O for 10 min at 40 °C. The sample was immersed in phosphoric acid, resulting in the formation of AAO nanopores [34, 35]. To achieve better pore ordering and uniformity, the sample was anodized for a second time under the same conditions.

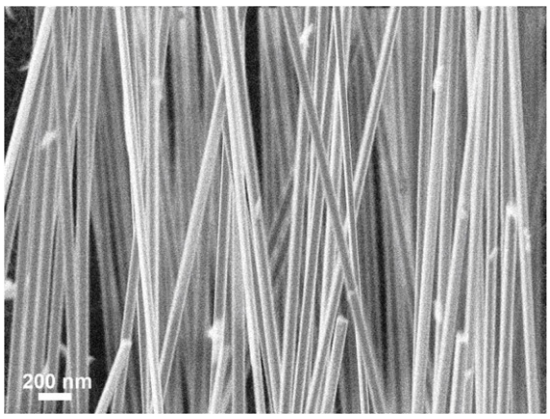

Figure 1. SEM image of silicon nanowires applied in the initial approach for insertion into nanopores. The average diameter of the nanowires is 70 ± 5 nm. The image was taken before surface modification of the antibodies. The scale bar is 200 nm.

2.4. Assembly protocol for nanopillar array

The nanowires were cleaned by immersing in 0.2 M NaOH for 10 min, 0.2 M HCl for 3 min, followed by washing with distilled water for 5 min and then dried. Nanowires were soaked in 10% amino-propyl-triethoxysilane (APTES) for 1 h and then dried with toluene for 30 min at room temperature. To remove unbound APTES molecules, nanowires were rinsed several times with toluene and acetone and dried in an oven at 120 °C for 1 h. For the immobilization of antibodies, 100 μl of anti-GNP antibody (10^{-5} mg ml^{-1}) was incubated with APTES-functionalized nanowires at room temperature for 30 min, followed by blocking with 1% (w/v) BSA for 1 h and washed thoroughly by phosphate buffered saline (PBS). The surface-functionalized nanowires were mixed with a pre-GNP-deposited nanopore array, followed by centrifugation at 30 000g for 30 min. The pre-deposition of 5 nm GNPs was performed by dropping the GNPs onto the nanopore array and incubating it in a total volume of 5 ml, which covered the top of the array, in a centrifugation tube for 10 min to allow for the proper sedimentation of the GNPs into the nanopores. The final concentration of the GNPs varied from 0 to 68.0 μM. Residual GNPs deposited on the top of AAO was removed by PBS washing. Antibody-conjugated nanowires were added to the top of the solution, which was then centrifuged at 30 000g for 30 min. The nanopore array was then washed thoroughly, dried under vacuum and examined via SEM.

2.5. Transmission electron microscopy (TEM)

Small pieces of unfixed tissue were fixed in 2.5% glutaraldehyde with 0.05 M sodium cacodylate buffered saline (pH 7.4) at room temperature for 2 h. The samples were sectioned into 100 nm sections using an ultra-microtome. The grids with ultrathin sections were post-stained with uranyl acetate for 30 min and then by lead acetate for 3 min. After the post-staining procedure, a thin layer of carbon was evaporated onto the grid surfaces. Ultrathin-sectioned material was examined with a JEOL 1400 and a 3200 FS TEM.

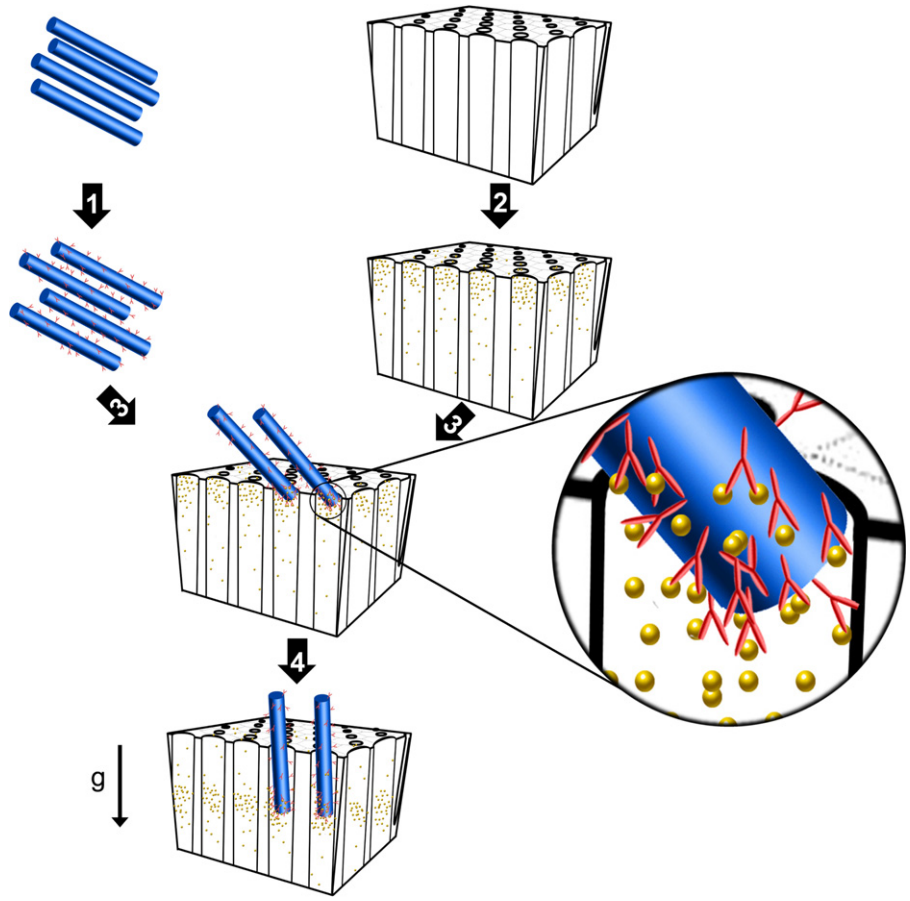

Figure 2. Schematic representation of the proposed hypothesis for inserting nanowires into nanopores. The AAO-processed nanopore array is first loaded with 5 nm GNPs. Silicon nanowires are synthesized, cross-linked with anti-GNP antibodies, and mixed with the GNP-loaded nanopore array, followed by centrifugation at 30 000*g* for 30 min. Antibody-conjugated nanowires can bind to GNPs and are pulled into the nanopores by centrifugation.

3. Results and discussion

Here, we propose a bio-guiding technique in which antibody–antigen binding is applied to assemble silicon nanowires and anodic aluminum oxide (AAO) nanopore arrays into an antireflective nanopillar array (figure 2). In this method, nanowires with a diameter of 70 nm are first cross-linked with an anti-gold nanoparticle (anti-GNP) antibody [36, 37] and then placed on the top of a nanopore array with a pore size of 115 nm [38, 39] on which GNP had been deposited, followed by centrifugation at 30 000*g* for 30 min. The binding of antibody and GNP is highly specific to size and surface composition [28, 29]. The antibody binds GNPs ranging from 3.5 to 6 nm and maximizes at 5 nm. The binding activity is blocked by 5 nm GNP but undisturbed in the presence of an excess amount of ZnO, TiO_2 and Fe_3O_4 nanoparticles. In the absence of antibody modification the insertion rate was virtually zero. However, an insertion success rate of 5.3% was achieved following the antibody-directed assembly protocol (figure 3(A)). The low insertion success rate indicated that factors other than the antibody and the GNP may need to be considered. For example, a broad size distribution was observed for unpurified nanowires (figure 1). Size variation of nanowires may play a pivotal role during insertion. The nanowires that had been successfully inserted were recovered which populated with a length of approximately 350 nm (figure 3(B)). We found nanoparticles scattered sparsely on the surfaces of these wires (figure 3(C)). Elemental analysis by EDS confirmed them to be GNPs (figure 3(D)). Interestingly, the density was much lower than in the GNP-saturated nanowires (figure 3(E)), indicating the loss of bound GNPs during the removal. Nanorods shorter than 350 nm were preferentially selected by the assembly protocol.

3.1. Optimization for aspect ratio

To investigate the effect of aspect ratio on the efficiency of insertion, silicon nanowires with aspect ratios of 5:1 (356 ± 127 nm in length), 8:1 (586±109 nm), 13:1 (892±97 nm), 16:1 (1152 ± 133 nm) and 23:1 (1612 ± 143 nm) were synthesized (figure 4), functionalized with the antibody, and assembled with GNP-deposited nanopore arrays. Nanowires with aspect ratios of 5 and 8 exhibited an insertion rate higher than 90% (figure 5). The insertion rate dropped to 21% for nanowires with an aspect ratio of 13, 5% for an aspect ratio of 16 and to 1.5% for an aspect ratio of 23. The sudden decrease in the insertion rate for an aspect ratio of 8:1 indicates that an aspect ratio lower than 8:1 leads to a lower energy barrier and is thus

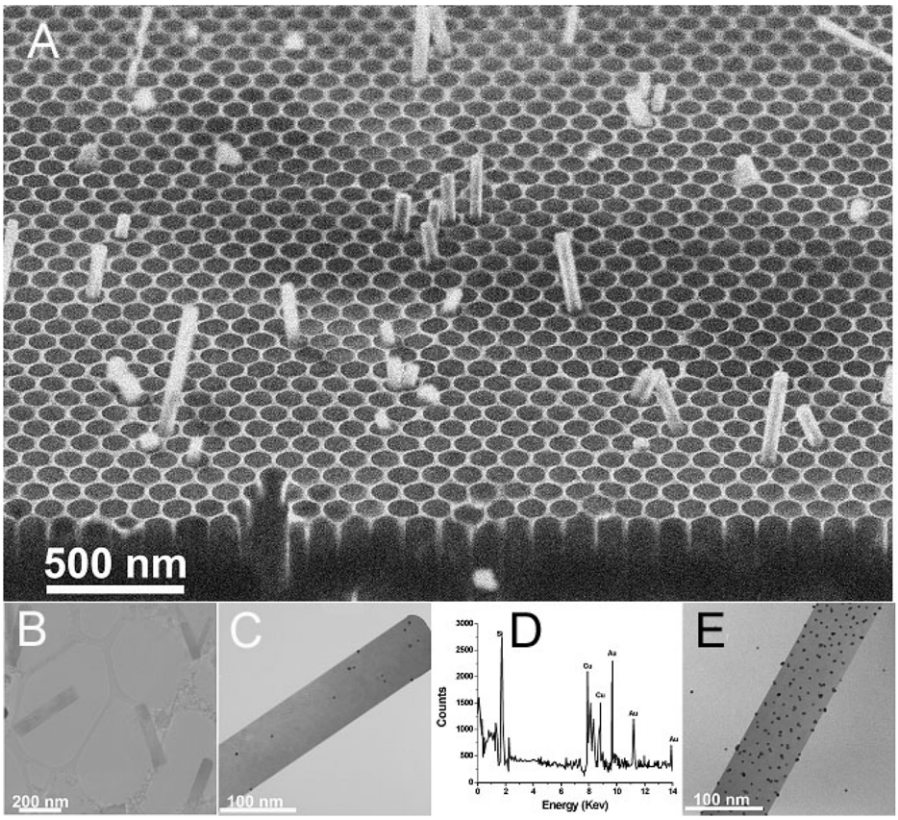

Figure 3. Electron microscopic characterization of a wire-in-pore array from unsorted nanowires. (A) SEM image of the inserted silicon nanowires in the nanopores of the array. (B), (C) TEM images of nanowires recovered from a wire-in-pore array. (D) Elemental analysis of the dark spots in attached nanowires by EDS was also performed. GNPs were identified by the presence of the characteristic peaks of gold. (E) GNPs bind to the surfaces of antibody-modified nanowires. The distribution of GNP-binding sites on the nanowires prior to the insertion was characterized by the binding reaction in the test tube. The GNP-binding sites were identified by the positions of GNPs.

a more likely outcome when using this procedure. It is likely that, during the course of insertion, nanowires formed a lever at the opening of pores with the rim of the opening serving as a pivot. The antibody–GNP interaction, as a driving force, overcame the disadvantageous leverage and pulled wires into the pores (figure 2). An aspect ratio lower than 8 would ensure a lower energy barrier and, thus, was preferentially selected in the experiment.

3.2. Factors that affected assembly efficiency

In addition to optimizing the insertion rate via selection of the aspect ratio, the insertion rate was also optimized through selection of the antibody and GNP concentrations. Nanowires with an aspect ratio of 5:1 were functionalized with an anti-GNP antibody at concentrations ranging from 10^{-8} to 10^{-3} g l^{-1} (figure 6). For those nanowires that were modified using an antibody at a concentration of 10^{-8} mg ml^{-1}, a 12% insertion rate was obtained. The insertion rate increased rapidly and plateaued at 95% for an antibody concentration of 10^{-4} mg ml^{-1}. Plateauing likely occurred due to the saturation of antibodies on the surface of the nanowires. As a control, the insertion rate was observed to be negligible in the presence of 10^{-2} mg ml^{-1} normal serum, indicating that the effect of an anti-GNP antibody is highly selective. Figure 7 shows the relationship between the insertion success rate and the GNP concentration. In the absence of GNPs, no insertion was observed. The insertion rate increases rapidly and reaches a plateau of 92% with the use of 40.8 μM GNPs. The presence of this plateau is likely due to the saturation of GNPs on the inner surfaces of the nanopore array near to the nanopore rims.

It should be noted that the affinity between the nanowires and nanopores alone is not sufficient for a successful assembly of nanopillar array. Creating an affinity environment in the nanopore array and differentiating the non-affinity environment outside the pores apparently drives nanowires into pores. For example, APTES modification of nanowires allowed for the deposition of nanowires on the surfaces of nanopores (figure 8). The APTES modification created uniform but non-selective affinity, while the pre-deposition of GNPs created a non-uniform affinity environment that differs between the inside and outside of nanopores. The deposited GNPs occupied and concentrated near the openings of nanopores (figure 8(A)). The deposited GNPs provided sufficient affinity to attract nanowires and facilitate their assembly.

During the process, the depth of nanowire insertion was proportional to the centrifugation time and reached a plateau after 30 min (figures 9(A) and (B)). Nanowires approximately 240 nm in length were inserted into pores after 30 min of centrifugation. SEM imaging indicated that the deposited

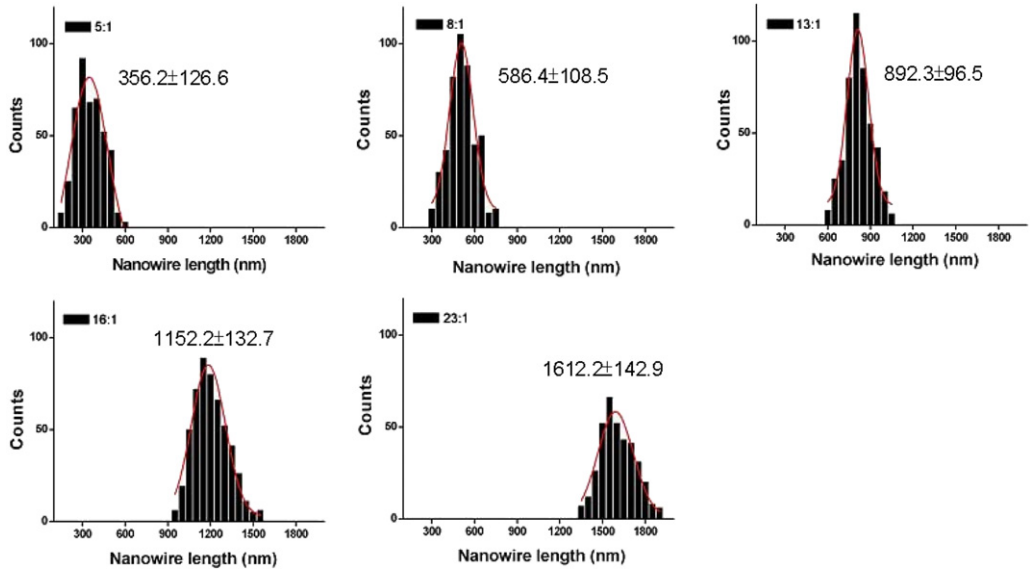

Figure 4. Size distribution of silicon nanowires purified at selected aspect ratios. Silicon nanowires 70 nm in diameter were synthesized and purified at ratios indicated by each plot. The measured aspect ratios were 5:1, 8:1, 13:1, 16:1 and 23:1 are 356 ± 127, 586 ± 108, 892 ± 96, 1152 ± 133 and 1612 ± 143, respectively.

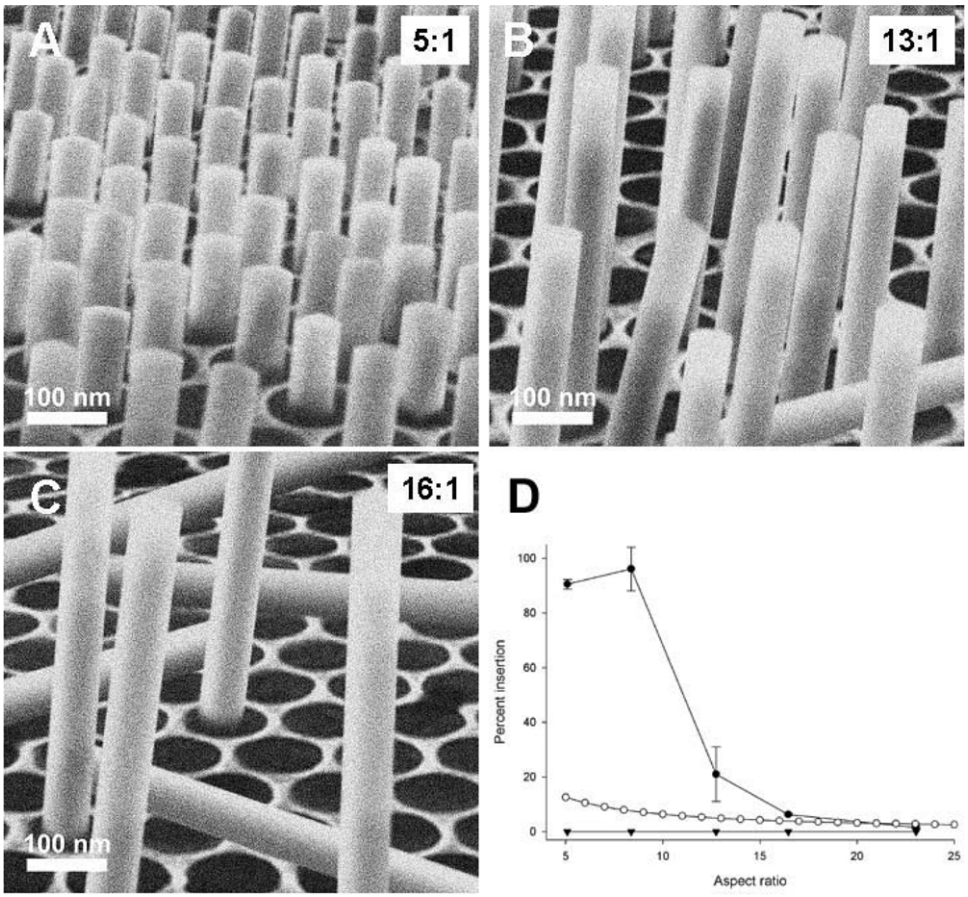

Figure 5. Effect of aspect ratio on the per cent insertion of nanowires. Nanowires are modified by 10^{-5} g l^{-1} anti-GNP antibodies and inserted into nanopores pre-deposited by 54.4 μM GNP. Representative images of aspect ratios at (A) 5:1, (B) 13:1 and (C) 16:1 are shown. (D) Per cent insertion versus aspect ratio. Prior to insertion, nanowires are cross-linked with anti-GNP antibodies (●) or with normal serum (○). All values represent the averages of six independent experiments. Values shown in the plot are mean ± standard deviation. The theoretical insertion rate is also shown (▼).

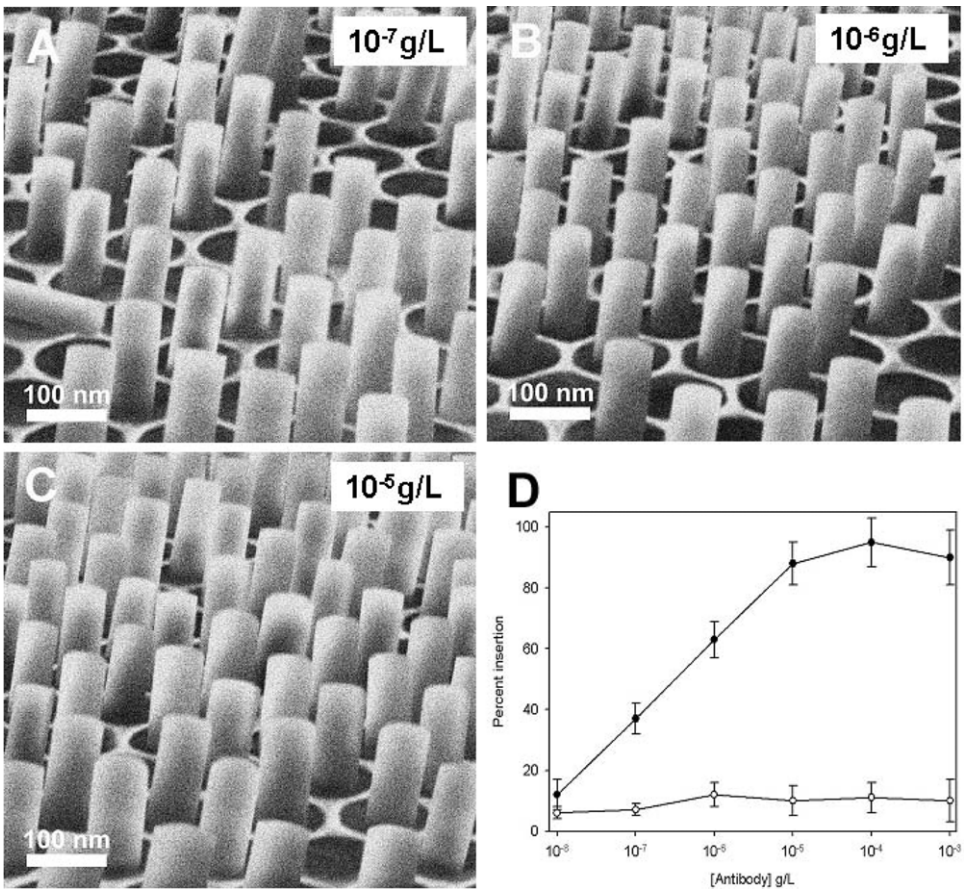

Figure 6. Effect of antibody concentration on the per cent insertion of nanowires. The insertion success rate in the wire-in-pore array was optimized by adjusting the concentrations of antibodies in the presence of 54.4 μM GNP. Nanowires with 5:1 aspect ratios were used. Representative images of antibody concentrations at (A) 10^{-7} g l^{-1}, (B) 10^{-6} g l^{-1} and (C) 10^{-5} g l^{-1} are shown. (D) Insertion success rate (filled circles) and per cent nanowires outside of pores (open circles) are plotted against antibody concentration. In the presence of 10^{-8} mg ml^{-1} antibodies and 54.4 μM GNP, an 11% insertion rate was obtained. The insertion rate increases rapidly and reaches a plateau of 95% at 10^{-5} mg ml^{-1} antibodies. For the control experiment, insertion was performed in the presence of 10^{-2} mg ml^{-1} normal serum at 54.4 μM GNP. The insertion rate was zero, indicating that the effect of antibodies is highly selective. At all concentrations of antibodies, nanowires outside of the pore array remain almost unchanged at about 5–10% (open circles). All values represent the averages of six independent experiments. Values shown in the plot are mean ± standard deviation.

GNPs were concentrated near the openings of the nanopores. The interaction between AAO and GNPs is a nonspecific adsorption process and could be attributed to van der Waals forces. During the initial stage, the GNPs served as an attractive and guiding force that targeted the insertion of the nanowires. Centrifugation pushed the wires deeper in the pores. The sliding action of nanowires was very likely due to the weak and nonspecific van der Waals force between GNPs and AAO. Once the nanowires passed the opening area, the attractive force of the antibody–GNP interaction became a dragging force that held the nanowires near the opening and prohibited further penetration by the nanowires. The forces acting on the nanowires during insertion included a centrifugation force, water resistance, thermo-fluctuation, GNP/AAO interaction and an attracting/dragging force caused by antibody–GNP binding. The mass of a single nanowire is approximately 9×10^{-18} kg (dimensions: 70 nm in diameter and 350 nm in length). The centrifugation force at 30 000g is approximately 3 pN. A nanoparticle 500 nm in diameter experiences a 0.09 pN drag force as it moves through water at a velocity of 10 μm s^{-1}. We were unable to estimate the force from thermo-motion; however, the unbinding force for the antibody–antigen interaction is approximately 400 pN [40, 41], almost two orders of magnitude higher than the centrifugation force and sufficient to physically move and manipulate nanowires. To elucidate the contribution of the antibody–GNP interaction a simplified insertion model was proposed (figure 9(C)). Insertion of nanowire is valid when $F1 \times L1 = F2 \times L2$, where $F1$ and $F2$ are centrifugation forces at the mass centers of the outside and inside halves of the nanowire. $L1$ and $L2$ are corresponding displacement vectors from forces to fulcrum. When the end of the nanowire stands on the edge of the rim the insertion angle θ equals $\tan^{-1}(1/Ra)$, where Ra is the aspect ratio of the nanowires. Assume the orientation of nanowires is randomly distributed in the solution; the theoretical insertion rate is obtained as the ratio of θ divided by $\pi/4$ (figure 5(D)). For example, assuming the nanowire is 70 nm in diameter and 350 nm in length. $L1$ is $Io/2 \sin\theta$ and $L2$ is $d \cos\theta$ nm ($Io = 300$ nm, $d = 50$ nm). $F1$ and $F2$ are approximately 0.56 pN and

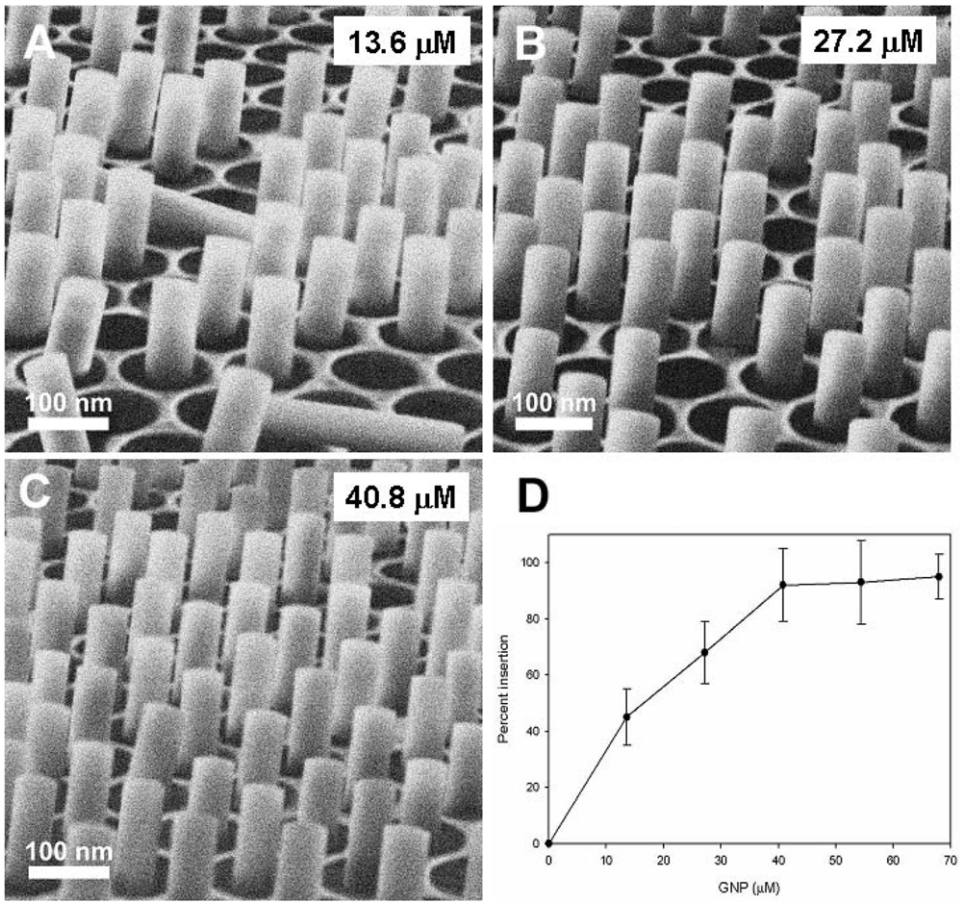

Figure 7. Effect of GNP concentration on the per cent insertion of nanowires. The insertion success rate of the wire-in-pore array was optimized by adjusting the concentrations of GNPs in the presence of 10^{-5} mg ml^{-1} antibodies. Nanowires with 5:1 aspect ratios were used. Representative images of GNP concentrations at (A) 13.6 μM, (B) 27.2 μM and (C) 40.8 μM are shown. (D) Insertion success rate is plotted against GNP concentration. The insertion rate increases rapidly and reaches a plateau of 92% at 40.8 μM GNP. The values represent the averages of six independent experiments. Values shown in the plot are mean $\pm$ standard deviation. In the absence of GNP, no insertion is observed.

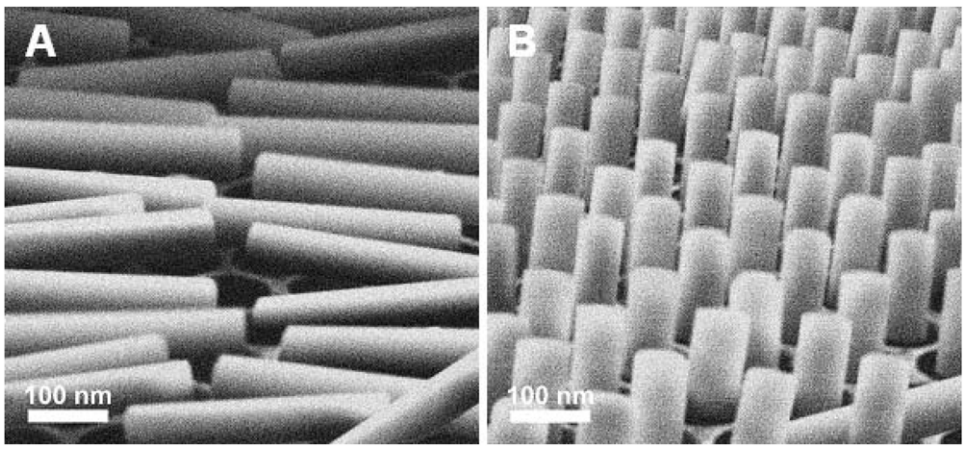

Figure 8. Effect of APTES modification on the per cent insertion of nanowires. Nanowires were functionalized by APTES and insertion was performed in GNP-deposited nanopores. The insertion success rate is virtually zero for APTES modification (left), while in the presence of anti-GNP antibodies, the per cent insertion is 95% (right).

0.44 pN, respectively. The interaction of antibody and GNP will be dominant and serve as a driving force that inserts the nanowire into the AAO nanopore. The theoretical insertion rate for nanowires with an aspect ratio of 8.4 is 7.6%. In the presence of antibody–GNP interaction, this rate is elevated to 96%. The enhancing effect decreased rapidly and approached

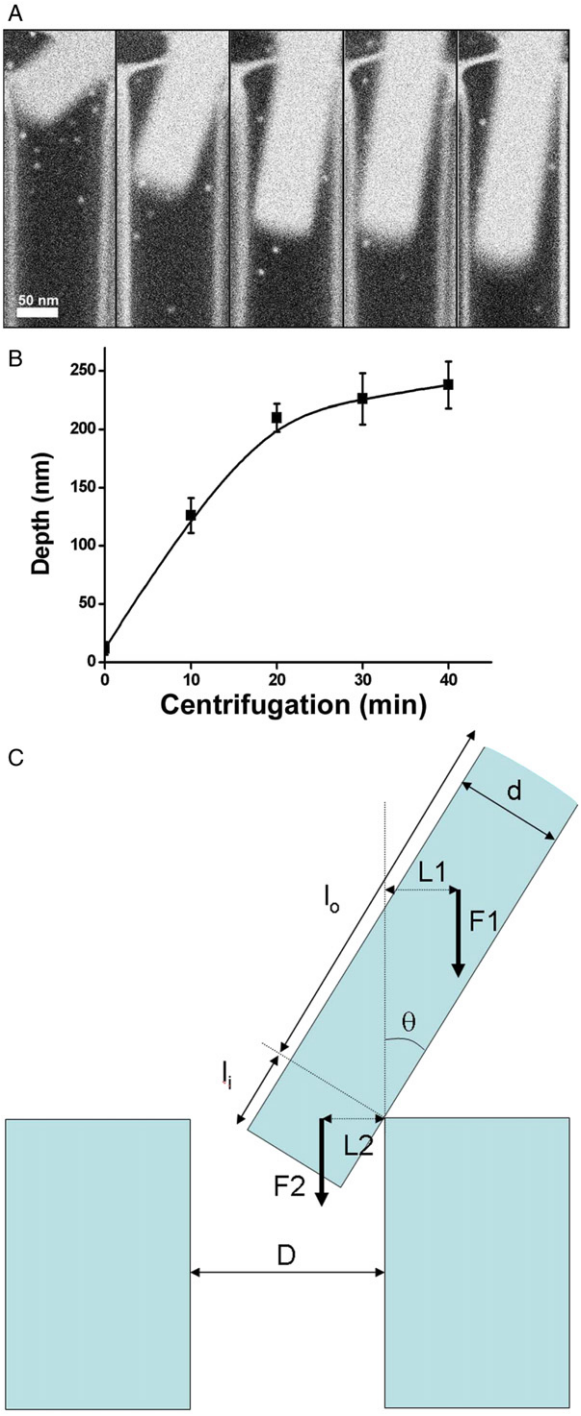

Figure 9. Effect of centrifugation time on the insertion depth of nanowires at 30 000*g* force. Nanowires with 5:1 aspect ratios were used (70 nm in diameter; 350 nm in length). (A) Representative SEM images of centrifugation time at 0, 10, 20, 30 and 40 min are shown. The bright spots near the rims of the nanopores represent GNPs. (B) Insertion depth is drawn versus centrifugation time. The insertion depth is time-dependent and reaches a plateau at 25 min of centrifugation. (C) Proposed model for the early stage of insertion. The front end of the nanowire touches the edge of the nanopore and forms a lever with the edge of the pore serving as a pivoting point. The nanowire inserts into nanopores with an insertion angle θ. $F1$ and $F2$ are centrifugation forces at the centers of the outside and inside halves of nanowires. $L1$ and $L2$ are corresponding displacement vectors from forces to fulcrum. Ii and Io indicate the length of nanowire inserted or left out. D: diameter of nanopore. d: diameter of nanowire.

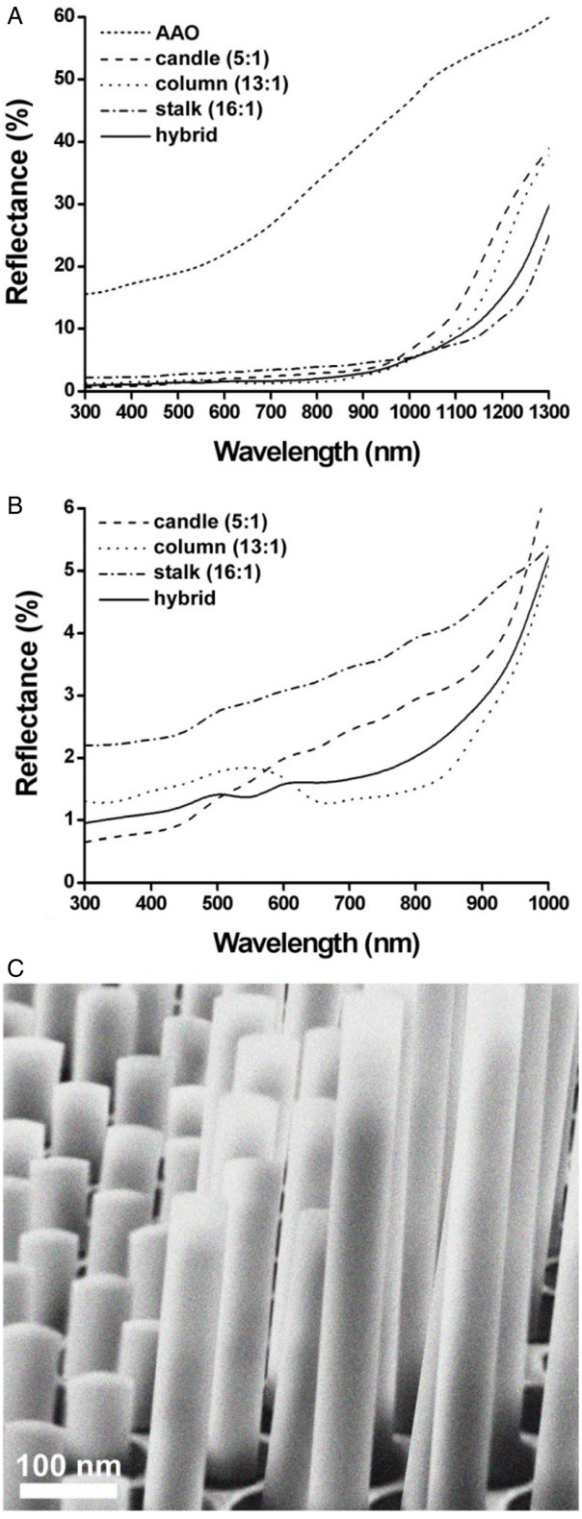

Figure 10. The hemispherical reflectance of nanopore arrays and nanopillar arrays. (A) The reflectance of a nanopore array (indicated by AAO), a candle-type nanopillar array, a column-type nanopillar array, a stalk-type nanopillar array and a hybrid nanopillar array. (B) The reflectance measurement from (A) expanded to visualize the difference in reflectance between the different types of nanopillar arrays. Please note that the wavelength range is narrower in (B) than in (A). (C) An SEM image of a hybrid nanopillar array that was assembled using a nanopore array and a 1:1:1 mixture of nanowires with aspect ratios of 5:1, 13:1 and 16:1.

zero when the aspect ratio is higher than 16. It is likely that the antibody–GNP interaction contributed to the early phase of insertion. The strength of the antibody–GNP interaction is not exceptional. Many biological molecules function with forces in this range. Consequently, forces such as those in receptor–ligand binding, enzyme–substrate interactions and chemical bonding using cross-linking agents could be effective for the bio-manipulation of nanowires. Bio-guided assembly can be facilitated via a specific interaction of conjugated biomolecules with nanowires. With the application of antibody–antigen binding, it is likely that forces operating on a molecular scale can be utilized to facilitate nanoscale manipulation.

3.3. Reflectance of nanopillar arrays

The reflectance of the nanopillar arrays was measured over a wavelength range of 300–1300 nm. Figure 10 shows the hemispherical reflectance of the nanopillar arrays assembled from AAO nanopore arrays and nanowires with aspect ratios of 5:1 (candle), 13:1 (column) and 16:1 (stalk). For column and stalk nanopillar arrays, an insertion rate of 85% was achieved by repeating the assembly processes. The AAO nanopore arrays exhibited a 15%–60% reflectance over the investigated wavelength range. For the nanopillar arrays, a low reflectance (less than 5%) was observed in the wavelength range of 300–950 nm. However, nanopillar arrays with various aspect ratios exhibited differing reflectance. The reflectance of the candle-type nanopillar arrays exhibited less than 2% reflectance over a wavelength range of 300–580 nm. The column-type nanopillar arrays exhibited less than 2% reflectance over a wider wavelength range, from 300 to 860 nm. The stalk-type nanopillar arrays were not as effective at reducing reflectance as the other array types; however, less than 5% reflectance was observed for wavelengths shorter than 950 nm. In general, the candle-type and column-type nanopillar arrays yielded a lower reflectance over a broader wavelength range, as compared to the stalk-type arrays. Nanopillar arrays with a mixture of nanowire aspect ratios would be expected to suppress reflections over a broader spectral range. Lithographic processing leads to the fabrication of nanopillar arrays that have constant pillar heights. However, it is possible to construct hybrid nanopillar arrays with custom pillar lengths through the use of the bio-guided assembly method. A hybrid nanopillar array was assembled from a nanowire mixture consisting of equal amounts of three different lengths of nanowires (figure 10(C)). A relatively low reflectance was observed over the wavelength range of 300–1000 nm, a result that is comparable to the result that was obtained for the column-type nanopillar array. However, a lower variation of reflectance with wavelength was observed. The antireflective performance of nanopillar arrays is tunable by optimizing the composition of the nanopillar arrays with an appropriate mixture of nanowires with various aspect ratios.

Nanowires have been demonstrated to function as excellent building blocks for high-performance electronic devices [42] and solar cells [24]. Physical techniques have previously been used to assemble one-dimensional nanostructures. For example, a microfluidic flow technique may be used to align nanowires with controllable periodicity [25, 26]. A hierarchical assembly of nanowires may be achieved through layer-by-layer manipulations of the microfluidic flow. In addition, the alignment of ZnO nanowires may be accomplished by alternating electric fields between electrodes [22, 23]. A device fabricated through use of this method has the potential to be utilized in such devices as diodes, switches and interconnects. Electric fields may also be applied to align metallic nanowires [23]. Magnetic fields may be used to orient and spin Ni-capped CuSn nanowires [24]. The incorporation of antibody–antigen affinity within the assembly process for nanopillar arrays provides a new resource for the manipulation of one-dimensional nanostructures.

The environmental impact of industrial processes is of increasing concern to society. Chemicals used in the semiconductor industry pose a wide range of health hazards, including toxicity, carcinogenicity and corrosiveness. These chemicals also have reactive and oxidizing properties that may facilitate global warming. In addition, semiconductor processing requires significant energy consumption, may contribute to water pollution and presents various electrical, mechanical and electromagnetic hazards. The use of bio-nanotechnology will greatly reduce hazardous chemical usage and energy consumption in the manufacturing process.

In summary, we have demonstrated the assembly of antireflective silicon nanopillar arrays from nanowires and nanopore arrays with the assistance of an antibody–antigen binding process. The antireflective property of nanopillar arrays can be fine-tuned through the selection of an appropriate mixture of nanowires with various aspect ratios. The bio-nano fabrication process holds promise for a reduction in the usage of hazardous chemicals and a saving of energy.

We also demonstrate here the bio-directed manipulation of nanowires to construct higher-level nanodevices using bottom-up fabrication. This is a time-saving and cost-effective process that does not use sophisticated semiconductor processing or expensive instruments. Based on the design scheme, the building blocks are not limited to Si nanowires or AAO nanopores. Nanowires or nanorods with proper modification can be inserted into pre-GNP-deposited pore arrays.

Acknowledgments

This study was supported in parts by the National Science Council grant 100-2923-B-009-001-MY3 and by ‘Aim for the Top University Plan’ of the National Chiao Tung University and Ministry of Education, Taiwan, ROC.

References

[1] Boal A K, Ilhan F, DeRouchey J E, Thurn-Albrecht T, Russell T P and Rotello V M 2000 Self-assembly of nanoparticles into structured spherical and network aggregates *Nature* **404** 746–8

[2] Collier C P, Vossmeyer T and Heath J R 1998 Nanocrystal superlattices *Annu. Rev. Phys. Chem.* **49** 371–404

[3] Harnack O, Pacholski C, Weller H, Yasuda A and Wessels J M 2003 Rectifying behavior of electrically aligned ZnO nanorods *Nano Lett.* **3** 1097–101

[4] Hayward R C, Saville D A and Aksay I A 2000 Electrophoretic assembly of colloidal crystals with optically tunable micropatterns *Nature* **404** 56–9

[5] Li M, Schnablegger H and Mann S 1999 Coupled synthesis and self-assembly of nanoparticles to give structures with controlled organization *Nature* **402** 393–5

[6] Mirkin C A 2000 Programming the assembly of two- and three-dimensional architectures with DNA and nanoscale inorganic building blocks *Inorg. Chem.* **39** 2258–72

[7] Murray C B, Kagan C R and Bawendi M G 1995 Self-organization of Cdse nanocrystallites into 3-dimensional quantum-dot superlattices *Science* **270** 1335–8

[8] Smith P A, Nordquist C D, Jackson T N, Mayer T S, Martin B R, Mbindyo J and Mallouk T E 2000 Electric-field assisted assembly and alignment of metallic nanowires *Appl. Phys. Lett.* **77** 1399–401

[9] Bentley A K, Trethewey J S, Ellis A B and Crone W C 2004 Magnetic manipulation of copper–tin nanowires capped with nickel ends *Nano Lett.* **4** 487–90

[10] Huang Y, Duan X F, Wei Q Q and Lieber C M 2001 Directed assembly of one-dimensional nanostructures into functional networks *Science* **291** 630–3

[11] Yu G H, Cao A Y and Lieber C M 2007 Large-area blown bubble films of aligned nanowires and carbon nanotubes *Nature Nanotechnol.* **2** 372–7

[12] Cui Y and Lieber C M 2001 Functional nanoscale electronic devices assembled using silicon nanowire building blocks *Science* **291** 851–3

[13] Fan Z *et al* 2010 Ordered arrays of dual-diameter nanopillars for maximized optical absorption *Nano Lett.* **10** 3823–7

[14] Lu Y and Lal A 2010 High-efficiency ordered silicon nano-conical-frustum array solar cells by self-powered parallel electron lithography *Nano Lett.* **10** 4651–6

[15] Sivakov V, Andra G, Gawlik A, Berger A, Plentz J, Falk F and Christiansen S H 2009 Silicon nanowire-based solar cells on glass: synthesis, optical properties, and cell parameters *Nano Lett.* **9** 1549–54

[16] Tian B, Zheng X, Kempa T J, Fang Y, Yu N, Yu G, Huang J and Lieber C M 2007 Coaxial silicon nanowires as solar cells and nanoelectronic power sources *Nature* **449** 885–9

[17] Huang Y F *et al* 2007 Improved broadband and quasi-omnidirectional anti-reflection properties with biomimetic silicon nanostructures *Nature Nanotechnol.* **2** 770–4

[18] Martinez J A, Misra N, Wang Y, Stroeve P, Grigoropoulos C P and Noy A 2009 Highly efficient biocompatible single silicon nanowire electrodes with functional biological pore channels *Nano Lett.* **9** 1121–6

[19] Shah A, Torres P, Tscharner R, Wyrsch N and Keppner H 1999 Photovoltaic technology: the case for thin-film solar cells *Science* **285** 692–8

[20] Xiang J, Lu W, Hu Y, Wu Y, Yan H and Lieber C M 2006 Ge/Si nanowire heterostructures as high-performance field-effect transistors *Nature* **441** 489–93

[21] Zhong Z, Wang D, Cui Y, Bockrath M W and Lieber C M 2003 Nanowire crossbar arrays as address decoders for integrated nanosystems *Science* **302** 1377–9

[22] Pui T S, Agarwal A, Ye F, Balasubramanian N and Chen P 2009 CMOS-compatible nanowire sensor arrays for detection of cellular bioelectricity *Small* **5** 208–12

[23] Yoon I, Kang T, Choi W, Kim J, Yoo Y, Joo S W, Park Q H, Ihee H and Kim B 2009 Single nanowire on a film as an efficient SERS-active platform *J. Am. Chem. Soc.* **131** 758–62

[24] Nicewarner-Pena S R, Freeman R G, Reiss B D, He L, Pena D J, Walton I D, Cromer R, Keating C D and Natan M J 2001 Submicrometer metallic barcodes *Science* **294** 137–41

[25] Salem A K, Chen M, Hayden J, Leong K W and Searson P C 2004 Directed assembly of multisegment Au/Pt/Au nanowires *Nano Lett.* **4** 1163–5

[26] Sioss J A, Stoermer R L, Sha M Y and Keating C D 2007 Silica-coated, Au/Ag striped nanowires for bioanalysis *Langmuir* **23** 11334–41

[27] Brown K R, Walter D G and Natan M J 2000 Seeding of colloidal Au nanoparticle solutions. 2. Improved control of particle size and shape *Chem. Mater.* **12** 306–13

[28] Chen Y-S, Hung Y-C, Chen K and Huang G S 2008 Detection of gold nanoparticles using immunoglobulin-coated piezoelectric sensor *Nanotechnology* **19** 495502

[29] Huang G S, Chen Y S and Yeh H W 2006 Measuring the flexibility of immunoglobulin by gold nanoparticles *Nano Lett.* **6** 2467–71

[30] Schwaber J and Cohen E P 1973 Human (times) mouse somatic cell hybrid clone secreting immunoglobulins of both parental types *Nature* **244** 444–7

[31] Engvall E and Perlmann P 1971 Enzyme-linked immunosorbent assay (ELISA). Quantitative assay of immunoglobulin G *Immunochemistry* **8** 871–4

[32] Van Weemen B K and Schuurs A H W M 1971 Immunoassay using antigen–enzyme conjugates *FEBS Lett.* **15** 232–6

[33] Kienberger F, Kada G, Mueller H and Hinterdorfer P 2005 Single molecule studies of antibody–antigen interaction strength versus intra-molecular antigen stability *J. Mol. Biol.* **347** 597–606

[34] Kim B, Park S, McCarthy T J and Russell T P 2007 Fabrication of ordered anodic aluminum oxide using a solvent-induced array of block-copolymer micelles *Small* **3** 1869–72

[35] Schwirn K, Lee W, Hillebrand R, Steinhart M, Nielsch K and Gosele U 2008 Self-ordered anodic aluminum oxide formed by H_2SO_4 hard anodization *ACS Nano* **2** 302–10

[36] Huber R and Bennett W S 1987 Antibody-antigen flexibility *Nature* **326** 334–5

[37] Skinner K, Dwyer C and Washburn S 2006 Selective functionalization of arbitrary nanowires *Nano Lett.* **6** 2758–62

[38] Kachroo A, Schopfer C R, Nasrallah M E and Nasrallah J B 2001 Allele-specific receptor–ligand interactions in Brassica self-incompatibility *Science* **293** 1824–6

[39] Rini J M, Schulze-Gahmen U and Wilson I A 1992 Structural evidence for induced fit as a mechanism for antibody-antigen recognition *Science* **255** 959–65

[40] Allen S, Chen X Y, Davies J, Davies M C, Dawkes A C, Edwards J C, Roberts C J, Sefton J, Tendler S J B and Williams P M 1997 Detection of antigen-antibody binding events with the atomic force microscope *Biochemistry* **36** 7457–63

[41] Lee C-K, Wang Y-M, Huang L-S and Lin S 2007 Atomic force microscopy: determination of unbinding force, off rate and energy barrier for protein–ligand interaction *Micron* **38** 446–61

[42] Merkel R, Nassoy P, Leung A, Ritchie K and Evans E 1999 Energy landscapes of receptor–ligand bonds explored with dynamic force spectroscopy *Nature* **397** 50–3